CHEMISTRY OF MATERIALS
Article

Chem. Mater. **2010,** *22,* 6075–6084 6075
DOI:10.1021/cm1014866

Magnetoelectric Perovskite-Spinel Bilayered Nanocomposites Synthesized by Liquid-Phase Deposition

Amin Yourdkhani, Armando K. Perez, Cuikun Lin, and Gabriel Caruntu*

Advanced Materials Research Institute, University of New Orleans, 2000 Lakeshore Dr., New Orleans, Louisiana 70148, United States

Received May 27, 2010. Revised Manuscript Received October 4, 2010

Highly uniform bilayered perovskite-spinel hybrid nanostructures were deposited on glass and $LaNiO_3$-buffered (100) silicon substrates at almost-ambient temperatures via the liquid-phase deposition (LPD) method. Field-emission scanning electron microscopy (FE-SEM) and atomic force microscopy (AFM) evidenced that the perovskite and spinel layers are constructed by arrays of densely packed nanoparticles with uniform sizes. The bilayered nanocomposites exhibit both piezoelectricity and ferrimagnetism at room temperature. The value of the static piezoelectric coefficient of the $PbTiO_3$ (PTO) film was 14.1 pm/V, whereas the values of the saturation magnetization were 234.4 and 223.2 emu/cm^3 for the $PbTiO_3-Co_{0.32}Fe_{2.68}O_4$ (CFO) and $PbTiO_3-Ni_{0.66}Fe_{2.34}O_4$ (NFO), respectively. The coercivity of the nanocomposite decreased by 12.11% for the PTO−CFO, whereas, for the PTO−NFO, it increased by 20%, with respect to the coercivity values of the pristine ferrite films, which is the result of a magnetoelectric coupling between the two dissimilar layers in the nanocomposite. Additional evidence about a stress-induced magnetoelectric coupling in these bilayered structures was provided by Raman spectroscopy, which showed that, under a magnetic field, the vibrational modes of the nanocomposite are altered by the deformation of the top ferrite layer. In turn, this will generate a stress at the shared interface, thereby leading to a shift toward higher wavenumbers of the Raman bands of both the perovskite and spinel phases.

1. Introduction

Recent advances in miniaturization in electronics and computing generated a surge of interest in magnetoelectric (ME) ceramic nanocomposites, because they exhibit a strong room-temperature ME effect that can be potentially used in various applications in magnetic data storage, spintronics, and sensing.[1] ME nanocomposites are hybrid architectures that consist of a ferromagnetic and a ferroelectric phase, coupled together by a strain. Upon application of an electric field, the ferroelectric phase, which has electrostrictive properties, will respond to the external stimulus by changing its physical dimensions. Therefore, the induced stress is transmitted to the magnetostrictive phase through the shared interface, eventually leading to a change in its magnetization. Among the most studied magnetoelectric nanocomposites are those obtained by combining a ferromagnetic/ferrimagnetic spinel (MFe_2O_4) with a ferroelectric perovskite (ABO_3). This is because both spinels and perovskites have high chemical, thermal, and mechanical stabilities and form a limited number of secondary phases when mixed together. One of the possible geometries in which these phases can be assembled is a horizontal multilayered structure consisting of alternate layers of a spinel and a perovskite material. When the oxide phases are single crystalline, their growth during the formation of hybrid architectures takes place epitaxially, as a result of the commensurability of their lattice (lattice mismatch of $< 5\%$), thereby leading to strong interfacial coupling between the spinel and perovskite phases. Last, but not least, interfacing a ferroelectric with a ferromagnetic material in a planar geometry will greatly simplify the chip integration required for miniaturization of electronics and will minimize the leakage currents, because of the high resistivity of the ferrites, preventing the composites from electric breakdown during the poling process. Thus, perovskite-spinel nanocomposite layered structures are very attractive for the design of many functional devices including

*Author to whom correspondence should be addressed. E-mail: gcaruntu@uno.edu.

(1) (a) Petrov, V. M.; Srinivasan, G.; Bichurin, M. I.; Gupta, A. Phys. Rev. B **2007**, *75*, No. 224407. (b) Lu, J.; Pan, D. A.; Bai, Y.; Su, Y. J.; Qiao, L. J. *IEEE Trans. Magn.* **2008**, *44*(9), 2127–2129. (c) Bichurin, M. I.; Petrov, V. M.; Petrov, R. V.; Kapralov, G. N.; Kiliba, Y. V.; Bukashev, F. I.; Smirnov, A. Y.; Tatarenko, A. S. *Ferroelectrics* **2002**, *280*, 377–384.

(2) (a) Srinivasan, G.; Tatarenko, A. S.; Bichurin, M. I. *Electron. Lett.* **2005**, *41*(10), 596–598.(b) Dong, S. X.; Zhai, J. Y.; Xing, Z. P.; Li, J.-F.; Viehland, D. Appl. Phys. Lett. **2005**, *86*, No. 102901. (c) Tatarenko, A. S.; Gheevarughese, V.; Srinivasan, G. *Electron. Lett.* **2006**, *42*(9), 540–541.(d) Tatarenko, A. S.; Srinivasan, G.; Bichurin, M. I. Appl. Phys. Lett. **2006**, *88*, No. 183507. (e) Fetisov, Y. K.; Srinivasan, G. Appl. Phys. Lett. **2006**, *88*, No. 143503. (f) Srinivasan, G.; Tatarenko, A. S.; Mathe, V.; Bichurin, M. I. *Eur. Phys. J. B* **2009**, *71*(3), 371–375. (g) Filippov, D. A.; Bichurin, M. I.; Petrov, V. M.; Laletin, V. M.; Srinivasan, G. *Phys. Solid State* **2004**, *46*(9), 1674–1680.(h) Nan, C.-W.; Bichurin, M. I.; Dong, S. X.; Viehland, D.; Srinivasan, G. J. Appl. Phys. **2008**, *103*, No. 031101.

Published on Web 10/27/2010

controlled phase shifters, transducers, reading/writing devices in magnetic data storage, spin transistors, broadband magnetic field sensors, magnetoelectric memory cells, and magnetically controlled electro-optic or piezoelectric devices.[2] Multilayered $MFe_2O_4-ABO_3$ nano structures have been fabricated almost exclusively via physical methods, including pulsed-laser deposition (PLD),[3] laser molecular beam epitaxy (LMBE),[4] or radio frequency (rf) sputtering.[5] Although these techniques yield highly uniform, epitaxial films, they are restricted to surfaces with simple morphologies and require highly pure targets and expensive equipment. Fontcuberta and co-workers have grown nanocomposite films with the nominal composition $0.35CoFe_2O_4-0.65BaTiO_3$ onto (001) Nb-doped $SrTiO_3$ single crystals via rf sputtering. They observed a decrease in the dielectric losses as the thickness of the films decreased and as the synthesis temperature increased from 750 °C to 850 °C.[6] Srinivasan and co-workers have fabricated laminate structures using the so-called "tape casting technique",[7] whereas Hao and co-workers prepared 40-, 60-, 80-, and 100-nm-thick $CoFe_2O_4$ films deposited onto 100-nm-thick $BaTiO_3$ via molecular beam epitaxy.[8]

Solution-based approaches are very attractive for the design of perovskite-spinel magnetoelectric nanocomposites, because they allow mixing of the precursors at the atomic scale, which can potentially enhance the coupling between the two phases. Also, they use relatively low processing temperatures, which can significantly reduce the diffusion pathways of the molecular species, thereby preventing the formation of unwanted, secondary phases. Despite these advantages, chemical methods have been rarely used in the fabrication of magnetoelectric multilayers. Recently, Jia and co-workers prepared self-assembled epitaxial $BaTiO_3-NiFe_2O_4$ thin-film nanocomposites via a spin-coating process, using solutions of the metal precursors mixed with ethylenediaminetetraacetic acid (EDTA) and polyethyleneimine, followed by a heat treatment at 950 °C.[9] A simple, environmentally benign, highly efficient and easily scalable chemical deposition method yielding highly uniform metal oxide thin films is the so-called "liquid-phase deposition" (LPD). This approach exploits the slow hydrolysis of supersaturated solutions of metal fluoro-complexes at low temperature, whereby the F^- ions in the inner coordination sphere of the metal are progressively replaced by OH^- ions and/or water molecules.

$$MF_n^{(n-2m)-} + mH_2O \rightleftharpoons MO_m + nF^- + 2mH^+ \quad (1)$$

$$H_3BO_3 + 4HF \rightleftharpoons BF_4^- + H_3O^+ + 2H_2O \quad (2)$$

The hydrolysis reaction can be shifted to the right side upon the addition of a fluoride scavenger such as H_3BO_3, which forms water-soluble complexes with the F^- ions. Initially developed for the deposition of binary oxides, such as TiO_2,[10] SiO_2,[11] ZrO_2,[12] SnO_2,[13] Fe_2O_3,[14] and NiO,[15] the LPD method was rapidly extended to the deposition of complex oxides, such as perovskite titanates ABO_3 (A = Ba, Sr, and Pb).[16] Recently, our group has successfully used this methodology for the deposition of highly uniform transition-metal ferrite films with tunable chemical composition and controllable magnetic properties.[17] In this work, we describe an alternative soft-solution route for the fabrication of layered magnetoelectric nanostructures using the LPD method. The synthesis and characterization of two types of bilayered structures consisting of $PbTiO_3$ as the ferroelectric phase and a hard (cobalt ferrite)/soft (nickel ferrite) transition-metal ferrite as the magnetostrictive materials are presented to exemplify the generality of this approach. However, because of its simplicity, this method can be virtually used for the design of any combination of perovskite-type titanate and transition-metal ferrite in a layered geometry, whereby the number of layers and their thickness can be easily controlled upon properly adjusting the number of deposition steps and the deposition time, respectively.

2. Experimental Section

2.1. Chemical Deposition of Metal Oxide Thin Films. All experiments were performed in an open atmosphere, using a magnetic hot plate (IKA Works, Inc.) that was equipped with a temperature controller and a pH electrode. $PbTiO_3$ and MFe_2O_4 (M = Co, Ni) thin films were deposited from treatment solutions prepared by dissolving reagent-grade-purity chemicals (Alfa Aesar) in deionized water (18 MΩ) obtained from a Barnstead Nanopure water purification system. Both perovskite and spinel thin films were deposited on highly doped (100)

(3) (a) Chaudhuri, A. R.; Krupanidhi, S. B.; Mandal, P.; Sundaresan, A. J. Appl. Phys. **2009**, *106*, No. 054103. (b) Dix, N.; Muralidharan, R.; Caicedo, J. M.; Hrabovsky, D.; Fina, I.; Fabrega, L.; Skumryev, V.; Varela, M.; Guyonnet, J.; Paruch, P.; Sanchez, F.; Fontcuberta, J. *J. Magn. Magn. Mater.* **2009**, *321*(11), 1790–1794.(c) Li, J. H.; Levin, I.; Slutsker, J.; Provenzano, V.; Schenck, P. K.; Ramesh, R.; Ouyang, J.; Roytburd, A. L. Appl. Phys. Lett. **2005**, *87*, No. 072909.
(4) (a) Zhu, J.; Zhou, L. X.; Huang, W.; Li, Y. Q.; Li, Y. R. *J. Cryst. Growth* **2009**, *311*(12), 3300–3304. (b) Schlom, D. G.; Chen, L. Q.; Pan, X. Q.; Schmehl, A.; Zurbuchen, M. A. *J. Am. Ceram. Soc.* **2008**, *91*(8), 2429–2454.
(5) Bai, W.; Meng, X. J.; Yang, J.; Lin, T.; Zhang, Q. X.; Ma, J. H.; Sun, J. L.; Chu, J. H. J. Phys. D−Appl. Phys. **2009**, *42*, No. 145008.
(6) Fina, I.; Dix, N.; Laukhin, V.; Fabrega, L.; Sanchez, F.; Fontcuberta, J. *J. Magn. Magn. Mater.* **2009**, *321*(11), 1795–1798.
(7) Srinivasan, G.; Hayes, R.; Bichurin, M. I. *Solid State Commun.* **2003**, *128*(6−7), 261–266.
(8) Huang, W.; Zhu, J.; Zeng, H. Z.; Wei, X. H.; Zhang, Y.; Li, Y. R.; Hao, J. H. *Scr. Mater.* **2008**, *58*(12), 1118–1120.
(9) Luo, H. M.; Yang, H.; Bally, S. A.; Ugurlu, O.; Jain, M.; Hawley, M. E.; McCleskey, T. M.; Burrell, A. K.; Bauer, E.; Civale, L.; Holesinger, T. G.; Jia, Q. X. *J. Am. Chem. Soc.* **2007**, *129*(46), 14132.
(10) Aoi, Y.; Kambayashi, H.; Kamijo, E.; Deki, S. *J. Mater. Res.* **2003**, *18*(12), 2832–2836.
(11) Chou, J. S.; Lee, S. C. *Appl. Phys. Lett.* **1994**, *64*(15), 1971–1973.
(12) Cho, D. H.; Mizuhata, M.; Deki, S. *J. Ceram. Soc. Jpn.* **2007**, *115* (1346), 608–611.
(13) Nakata, A.; Mizuhata, M.; Deki, S. *Electrochim. Acta* **2007**, *53*(1), 179–185.
(14) Deki, S.; Aoi, Y.; Okibe, J.; Yanagimoto, H.; Kajinami, A.; Mizuhata, M. *J. Mater. Chem.* **1997**, *7*(9), 1769–1772.
(15) Lee, M. K.; Fan, C. H. *J. Electrochem. Soc.* **2009**, *156*(10), D395–D399.
(16) (a) Lee, M. K.; Liao, H. C.; Tung, K. W.; Shih, C. M.; Shih, T. H. *J. Phys. D−Appl. Phys.* **2002**, *35*(1), 61–64. (b) Hsu, M.-C.; Sun, Y.-M.; Leu, I.-C.; Hon, M.-H. *Appl. Surf. Sci.* **2007**, *253*(18), 7639–7644.
(17) (a) Caruntu, G.; Bush, G. G.; O'Connor, C. J. *J. Mater. Chem.* **2004**, *14*(18), 2753–2759. (b) Caruntu, G.; Newell, A.; Caruntu, D.; O'Connor, C. J. *J. Alloys Cmpd.* **2007**, *434*, 637–640.

silicon wafers with a resistivity of 0.05 Ω cm and commercial nonalkali glass plates (Corning No. 7059). Since the glass melts at temperatures above 600 °C, only the perovskite films deposited on silicon were annealed at 750 °C. Prior to deposition, the substrates were cleaned with a mixture of acetone and ethanol (50:50 w/w) and blow-dried with compressed argon. A 200-nm $LaNiO_3$ bottom electrode was spin-coated on the Si substrates, using a 0.4 M solution of $La(NO_3)_3$ and $Ni(ac)_2$ dissolved in ethanol, according to a procedure similar to that proposed by Meng et al.[18] The precursor solution was spin-coated at 3500 rpm for 30 s, and the resulting films were dried at 150 °C for 2 h, to allow removal of the solvent, and subsequently at 700 °C for 2 h in an open atmosphere. In addition to serving as a bottom electrode, the $LaNiO_3$ buffer layer can substantially minimize the clamping effect exerted by the substrate, ultimately leading to the enhancement of the ME effect.[19]

(*a*). *Deposition of $PbTiO_3$ Thin Films*. The deposition of perovskite films was performed by adapting the experimental procedure proposed by Hsu and co-workers.[20] In a typical experiment, three individual solutions containing 1 mmol of $Ba(NO_3)_2$ or $Pb(NO_3)_2$, 1 mmol of $(NH_4)_2TiF_6$, and 3 mmol of H_3BO_3 were mixed together, and water was added to a final volume of 100 mL. Deposition of the $PbTiO_3$ (PTO) thin films was performed in treatment solutions whose initial pH varied between 5.2 and 5.6, depending on the pH of the deionized water and decreased slowly to 4.1−4.7 after the deposition of the films. High-quality nanoparticle-based perovskite thin films with variable thicknesses were obtained by soaking the substrates in the treatment solution at 45 °C for a period of time, typically varying between 1 h and 4 h. After the deposition, the substrates were removed, rinsed and cleaned ultrasonically with distilled water, dried with a N_2 flow, and heat-treated at 750 °C in an open atmosphere for 3 h, followed by natural cooling to room temperature.

(*b*). *Deposition of MFe_2O_4 (M = Co, Ni) Thin Films*. The iron source used in the deposition of the MFe_2O_4 thin films was a solution obtained by dissolving 0.25 g of FeO(OH) in 50 mL of 1 M $NH_4F \cdot HF$ aqueous solution. FeOOH was obtained by precipitating an aqueous solution of $Fe(NO_3)_3 \cdot 7H_2O$ with a diluted solution of ammonia. The solid product was subsequently filtered, washed, and dried at room temperature in an open atmosphere, to ensure the oxidation of the Fe^{2+} ions. A volume of 10 mL of the iron-containing solution was mixed with 40 mL of 0.5 M H_3BO_3 and 3 mL of 2.2 M $Co(NO_3)_2$ or $Ni(NO_3)_2$ with the formation of the treatment solution. Substrates were suspended vertically and kept in the treatment solution at 45 °C for 4 h for the $CoFe_2O_4$ (CFO) films and 6 h for the $NiFe_2O_4$ (NFO) films, respectively. The initial pH of the solutions typically ranged between 5.5 and 5.9 to decrease slowly over the course of the deposition to values between 3.9 and 4.4. After their removal from the reaction solution, the films were carefully rinsed, cleaned ultrasonically with distilled water, and dried under flow of nitrogen. To ensure the conversion of the metal hydroxides/oxyhydroxides into the spinel structure and the complete crystallization of the films, the thin-film samples were annealed in open air at a temperature of 600 °C, followed by a natural cooling to room temperature. Although, in this work, we report only on the design of bilayered perovskite-spinel structures, by sequentially dipping the substrates into treatment solutions that contain different types of metal salt precursors, one can design multilayered ceramic composites on a film-on-substrate geometry. The advantage of this method consists of its simplicity, high reliability, and flexibility in varying the number of layers, as well as their thickness, order of succession, and chemical composition.

2.2. Characterization of the Metal Oxide Thin Films. The surface morphology, chemical composition, and microstructure of the films were investigated with a LEO Model 1530VP FE-SEM system operating in low vacuum mode at an accelerating voltage of 200 kV and equipped with an energy-dispersive spectroscopy (EDS) detector. X-ray diffraction (XRD) experiments were performed in grazing-incidence mode (2°) with a Philips X'Pert System equipped with a curved graphite single-crystal monochromator (Cu Kα radiation). Patterns were recorded in a step scanning mode in the 2θ range of 15°−60° with a step of 0.02° and a counting time of 10 s. The angular range was restricted to 15°−60°, because of a very strong reflection of the Si substrate, which appears at ∼68° 2θ and obscures the peaks of the metal oxide films. The chemical composition of the layered structures was determined by energy-dispersive X-ray (EDX) analysis and inductively coupled plasma (ICP) spectroscopy with a Varian Model FT220s flame absorption spectrometer. The correlation coefficient used to calibrate the instrument was 0.99915, and the calibration error did not exceed 5%. The corresponding solutions were prepared by dissolving the films in 18% HCl and then diluting them to the required concentrations. The thickness of the films was examined by a spectral reflectance method with a Filmetrics Model F20 film thickness measurement system. Atomic force microscopy (AFM) images of the thin films were collected at room temperature with an Asylum Research MFP-3D atomic force microscope working in tapping mode and using commercial Si_3N_4 cantilevers with a force constant of 0.7 N/m. The piezoelectric properties of the perovskite films were measured with the same instrument, using a silicon tip coated with a platinum/iridium layer 20 nm thick. The piezoelectric signal of the samples was measured with the high-voltage PFM module of the MFP-3D AFM system, using an AC240TM cantilever that had a tetrahedral silicon tip coated with platinum/titanium. For the fabrication of layered capacitors, the gold top electrodes, with an area of 5 mm^2 and a thickness of 50 nm, were sputtered on the film samples, followed by the standard lithography process. Investigation of the magnetic properties of the ferrite films and ferrite/perovskite multilayered nanocomposites was performed with a Quantum Design Model MPMS-5S SQUID magnetometer working in the temperature range from 2 K to 300 K and generating a magnetic field up to 6 T. Room-temperature magnetic-field-assisted Raman scattering studies were performed with a Thermo-Fisher DXR dispersive Raman spectrometer in a conventional backward geometry using the λ = 532 nm line. The spectral resolution was 3 cm^{-1}. The scattered light was analyzed with a triple monochromator coupled with an optical microscope, which allows the incident light to be focused on the sample as a circular spot ∼2 μm in diameter. The power of the incident laser beam was relatively low (6 mW), to avoid film restructuring that was due to overheating from the laser source. Prior to collecting each Raman spectrum, samples were subjected to the action of a uniform, in-plane magnetic field with a maximum strength up to 2 kOe, using a variable-field magnetometry (VFM) device provided by Asylum Research, Inc.

(18) Meng, X. J.; Sun, J. L.; Yu, J.; Ye, H. J.; Guo, S. L.; Chu, J. H. *Appl. Surf. Sci.* **2001**, *171*(1−2), 68–70.
(19) He, H. C.; Ma, J.; Lin, Y. H.; Nan, C. W. J. Phys. D−Appl. Phys. **2009**, *42*, No. 095008.
(20) (a) Hsu, M. C.; Leu, I. C.; Sun, Y. M.; Hon, M. H. *J. Solid State Chem.* **2006**, *179*(5), 1421–1425. (b) Vopsaroiu, M.; Blackburn, J.; Cain, M. G. *J. Phys. D−Appl. Phys.* **2007**, *40*(17), 5027–5033.

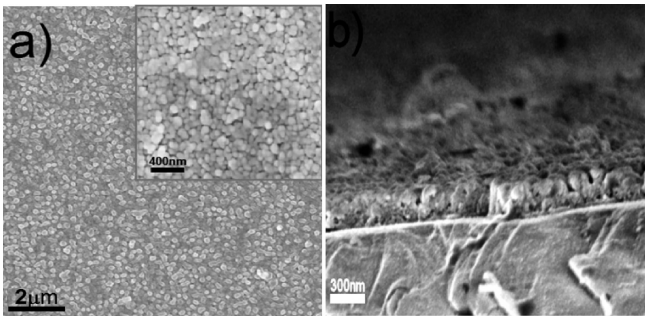

Figure 1. (a) Top view and (b) cross-sectional field-emission scanning electron microscopy (FE-SEM) images of an ~180-nm-thick $PbTiO_3$ layer obtained via liquid-phase deposition (LPD).

3. Results and Discussion

As previously described elsewhere,[17] the LPD process is based on the slow hydrolysis of metal oxyfluoro-complexes, which are converted to the corresponding hydroxides and/or oxyhydroxides, which form the as-deposited films. These stoichiometric mixtures of hydroxides/oxyhydroxides are usually amorphous and are transformed to the corresponding oxides upon heat treatment at temperatures above 500 °C. During our preliminary experiments, we have systematically observed that, at a high concentration of the precursors in the treatment solution, the addition of $Pb(NO_3)_2$ induces instant precipitation of the hydroxyl-containing metal species and no films are deposited onto the substrates. Other authors have suggested that the premature precipitation of the hydroxides can be prevented by adding few drops of diluted HNO_3 until the pH of the treatment solution is below 2.8.[1b,20b] However, when the pH of the treatment solution was brought below pH 3, no deposition was observed, even when the substrates were soaked in solution for 24 h at 45 °C. Upon optimizing the reaction conditions, mirror-like films could be obtained within 1−6 h without adjusting the pH and maintaining the concentration of the precursors in the treatment solution below 10^{-2} M. Therefore, the starting solution was clear at room temperature and visible precipitation was observed only 10−20 min after the solution reached the temperature of 45 °C. The treatment solution becomes turbid during the deposition due to the generation of fine particles, as a result of a homogeneous nucleation process. To minimize their high surface energy, these particles have the tendency to attach to all available surfaces, thereby leading to the formation of highly uniform, scratch-resistant nanoparticle-based films through a Volmer−Weber-type deposition mechanism.[21] All films have shown interference, rainbow-like color when exposed to the light, as a result of the different values of the refractive index of the substrate and the film. Figure 1 shows top-view (Figure 1a and inset) and cross-sectional (Figure 1b) FE-SEM images of a $PbTiO_3$ film deposited at 45 °C for 4 h, followed by a heat treatment at 750 °C for 6 h in air. The $PbTiO_3$ film is continuous, being constructed of densely packed grains with an average diameter of 77 nm. From the cross-sectional

(21) Gao, Y.; Koumoto, K. *Cryst. Growth Des.* **2005**, *5*(5), 1983–2017.

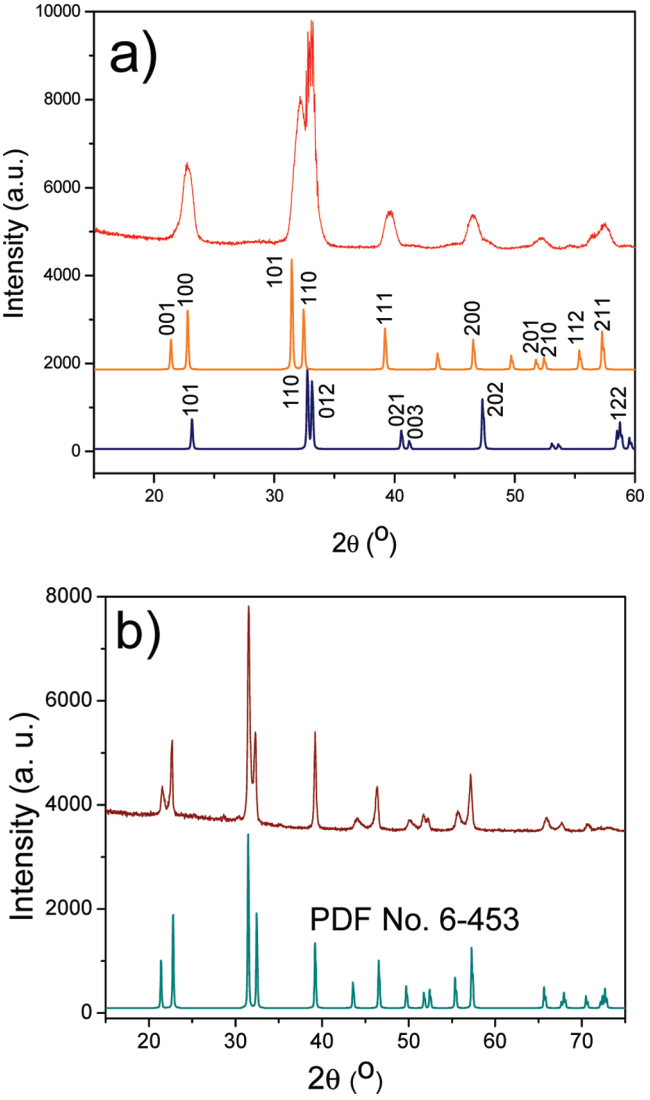

Figure 2. (a) X-ray diffraction (XRD) profiles of the $PbTiO_3$ film crystallized at 750 °C. The red curve represents the experimental pattern of the $PbTiO_3$ film, whereas the orange and blue curves represent the simulated curves of bulk $PbTiO_3$ (JCPDS File Card No. 6-452) and $LaNiO_3$ (JCPDS File Card No. 10-341), respectively. (b) Experimental XRD pattern of the $PbTiO_3$ powdered sample collected from the same experiment (dark red curve) and the simulated curves of bulk $PbTiO_3$ (blue-green curve).

FE-SEM image, we can observe that the $PbTiO_3$ film is uniform and has a thickness of ~180 nm. The EDX analysis of several randomly selected areas of the $PbTiO_3$ films indicated the presence of both Pb and Ti. The Pb/Ti molar ratio obtained from ICP spectrometry was 0.978:1, which indicates that the films are compositionally homogeneous and are almost stoichiometric. Our results, relative to the chemical composition of the perovskite films, are consistent with those of Hsu and co-workers, who suggested that the Ti^{4+} and Pb^{2+} ions are incorporated into a complex ion during hydrolysis and there is no loss of lead during the heat treatment.[20]

Figure 2a shows that the XRD pattern of the $PbTiO_3$ film heat-treated in air at 750 °C for 3 h exhibits well-defined peaks that can be classified into two categories. The first series matches well with those of $LaNiO_3$, whereas the second series of peaks belong to the tetragonal bulk

$PbTiO_3$ (macedonite, JCPDS File Card No. 6-452), indicating that the resulting ferroelectric film is chemically pure and highly crystalline. The similarity of the XRD patterns of the $LaNiO_3$ and $PbTiO_3$ layers, along with the strong (002) peak at 34° 2θ, originating from the Si substrate and the peak broadening due to the nanostructured nature of the $PbTiO_3$ film, made estimation of the crystallite size virtually impossible. Unlike the film, the $PbTiO_3$ powder collected after the deposition and subjected to the same heat treatment presents a XRD pattern with distinct peaks with no preferential orientation (Figure 2b), which confirms that the product of the deposition at 45 °C is tetragonal $PbTiO_3$. No impurities, such as pyrochlore $Pb_2Ti_2O_{7-y}$ or fluorite $Pb_{2+x}Ti_{2-x}O_{7-y}$, commonly encountered in the preparation of $PbTiO_3$ powders, were observed in the XRD pattern. The absence of a particular spatial orientation, either crystallographic or morphological, of the $PbTiO_3$ supports the existence of a homogeneous nucleation mechanism involved in the growth of the perovskite-like films via LPD. On the basis of XRD analysis, Hsu and co-workers suggested that the as-deposited hydroxide intermediate can be converted to a perovskite phase upon annealing for 30 min at temperatures as low as 550 °C. They observed that the product presented a small amount (5 wt %) of pyrochlore ($Pb_2Ti_2O_6$) impurity was eliminated by increasing the annealing temperature to 600 °C. It is worth mentioning that all samples annealed at temperatures below 750 °C contained an important amount (~40 wt %) of pyrochlore impurity. This phase is not ferroelectric and alters the piezoelectric properties of the samples. However, upon annealing the as-deposited films at 750 °C for 3 h in air, the pyrochlore phase can be completely converted to $PbTiO_3$. The lattice constants of the perovskite film crystallized onto the $LaNiO_3$ buffer layer were refined within a tetragonal cell, using the TREOR program.[22] These refined values of a = 3.908(7) Å and c = 4.123(1) Å are in very good agreement with those of the bulk material (a = 3.899(3) Å and c = 4.153(2) Å), further confirming the high quality of the films.

The piezoresponse hysteresis loops of the 180-nm-thick $PbTiO_3$ film are presented in Figure 3. Both the phase and amplitude curves confirm the existence of a switchable intrinsic lattice polarization in the PTO layer at room temperature. The film exhibits the well-known "butterfly-type" behavior for the variation of the amplitude versus the voltage with a maximum displacement of 1.2 nm at a driving voltage of E = +17.55 V. The effective value of the zero-field piezoelectric coefficient (d_{33}) of the $PbTiO_3$ film was calculated by fitting of the linear portion of the butterfly loop. It is well-known that the amplitude of the displacement of the tip (A) is proportional to the ac bias voltage (V_{ac}):

$$A = d_{33} V_{ac} Q$$

where Q is a proportionality factor that varies from 10 to 100 and accounts for the amplitude enhancement at the

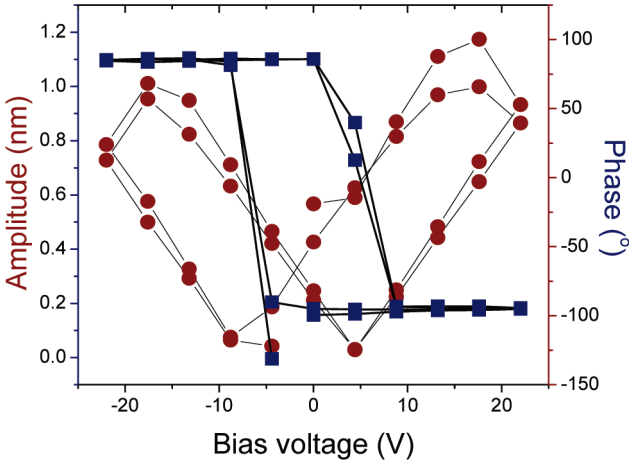

Figure 3. Local hysteresis loops of the phase (red curve) and amplitude (blue curve) of the piezoelectric signal of the ~180-nm-thick $PbTiO_3$ film.

tip−sample resonance. By considering the value of the proportionality factor in the lower end of this range, the magnitude of the piezoelectric coefficient of the PTO layer is d_{33} = 14.1 pm/V, a value that agrees well with those reported in the literature for layered $PbTiO_3$ nanostructures.[23] Two-dimensional (2-D) images of the 180-nm-thick $PbTiO_3$ film presented in Figure 4a and the inset of Figure 4a show that the perovskite film is free of cracks and has a uniform morphology over its entire surface (the scanned area was 10 μm × 10 μm), being constructed by densely packed spherical grains.

The root-mean-square (rms) roughness of the film was determined to be 9.7 nm. The piezoelectric force microscopy (PFM) contrast image of the same film without poling reveals a random distribution of bright and dark areas all across the film surface (see Figure 4b). The bright regions correspond to positive domains with the normal component of the polarization pointing toward the film surface, whereas the dark spots indicate areas where the polarization is oriented in the opposite direction. To design perovskite-spinel bilayered nanocomposites, a cobalt ferrite (CFO) layer was subsequently deposited onto the 180-nm-thick $PbTiO_3$ film by the same procedure. Similar to the case of the perovskite films, the spinel films were obtained upon a heat treatment at 600 °C in air of the as-deposited films, followed by the natural cooling to room temperature. ICP spectroscopy measurements of the solutions obtained by dissolving the film in a 10% HCl solution have indicated that, for the particular concentration of the $Co(NO_3)_2$ precursor in the treatment solution, the chemical composition of the ferrite film is $Co_{0.32}Fe_{2.68}O_4$, whereas their thickness, measured by the spectral reflectance technique was 193 nm. As seen in Figure 5, the top-view FE-SEM images of the PTO/CFO nanocomposite show that the surface of the CFO top layer is smooth and free of defects. Furthermore, the ferrite layer is constructed by densely packed spherically shaped grains with an average diameter of 90 nm (Figure 5b). The XRD

(22) Werner, P. E.; Eriksson, L.; Westdahl, M. J. Appl. Crystallogr. **1985**, *18*, 367−370.

(23) (a) Kighelman, Z.; Damjanovic, D.; Cantoni, M.; Setter, N. *J. Appl. Phys.* **2002**, *91*(3), 1495–1501. (b) Kim, Y. K.; Kim, S. S.; Shin, H.; Baik, S. *Appl. Phys. Lett.* **2004**, *84*(25), 5085–5087.

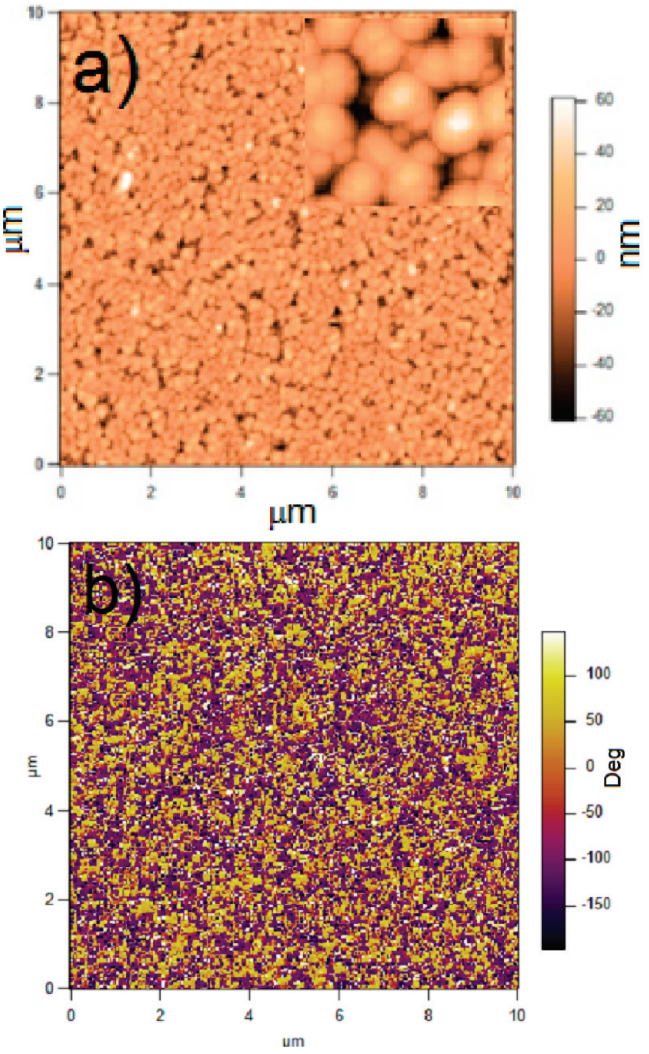

Figure 4. (a) Atomic force microscopy (AFM) image of the ~180-nm-thick $PbTiO_3$ film deposited at 45 °C. The inset shows a closeup of the same image, showing the size of the spherical particles constructing the film; (b) phase-contrast PFM image of the same film (10 μm × 10 μm).

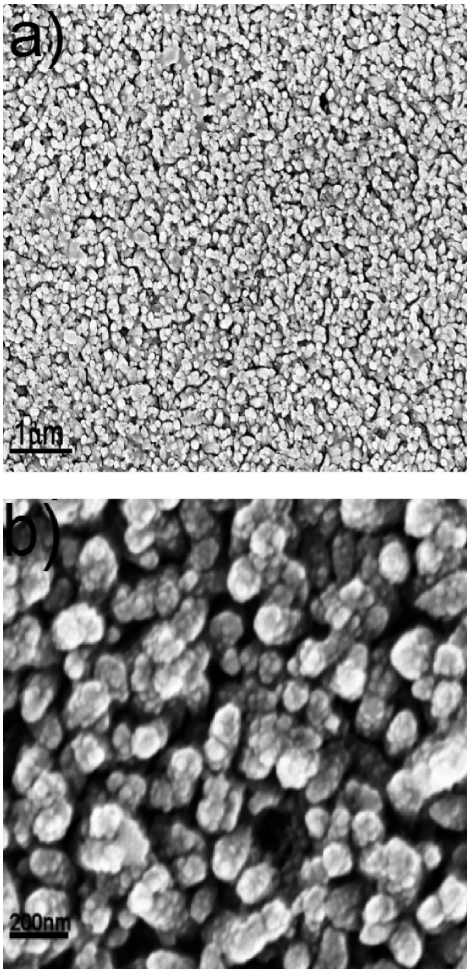

Figure 5. (a) FE-SEM image and (b) high-magnification FE-SEM view showing the typical morphology of the $CoFe_2O_4$ top layer of the PTO−CFO heteroepitaxial bilayered structure.

pattern of the PTO−CFO double-layered structure is dominated by the strong reflection at ~32° 2θ, corresponding to the $LaNiO_3$ buffer layer (Figure 6a). However, relatively strong peaks ascribed to the $PbTiO_3$ film, as well as a small peak at 35.8° 2θ, corresponding to the most intense reflection of the bulk $CoFe_2O_4$ spinel structure (JCPDS PDF No. 1-1121), can be easily observed, confirming the formation of a perovskite-spinel bilayered structure. Since the relatively intense peaks corresponding to the silicon substrate and the perovskite phases obscure those of the spinel phase, to determine if the ferrite film was single-phase, we investigated the XRD pattern of a $CoFe_2O_4$ thin film deposited onto a glass substrate under the same experimental conditions. As seen in Figure 6b, the XRD pattern suggests that the CFO film is polycrystalline, with no preferential orientation, and is chemically pure. The refined unit-cell parameter of the film annealed at 600 °C was a = 8.39(1) Å, which is close to the value of the bulk standard $CoFe_2O_4$. Figure 7a displays the surface morphology of the CFO film forming the top layer of the PTO−CFO perovskite-spinel heteroepitaxial bilayered structure obtained via AFM. The film has a smooth surface and consists of a continuous array of small and uniform grains, with an average diameter of 98 nm, which is in excellent agreement with the results obtained from electron microscopy. The rms roughness for the entire measured area was 34 nm. The magnetic force microscopy (MFM) image of the film (Figure 7b) exhibits several regions with a bright−dark contrast, indicating the existence of magnetic domains with upward and downward orientation of the magnetization. The magnetic properties of the PTO−CFO bilayered structure were measured by SQUID magnetometry. Hysteresis loops presented in Figure 8 indicate that the samples present a strong magnetic signal at room temperature and neither the PTO−CFO nanocomposite nor the pure CFO films reach saturation at a magnetic field of 8 kGauss. A negligible variation of the coercivity was noticed when the samples were measured with the magnetic field oriented parallel (in-plane) and perpendicular (out-of-plane) to the film surface, suggesting that they possess a randomly oriented magnetic anisotropy. The coercivity increased from 1.82 kOe to 13.39 kOe when the temperature of the in-plane measurement was decreased from 300 K to 5 K. The room-temperature coercivity of the PTO−CFO

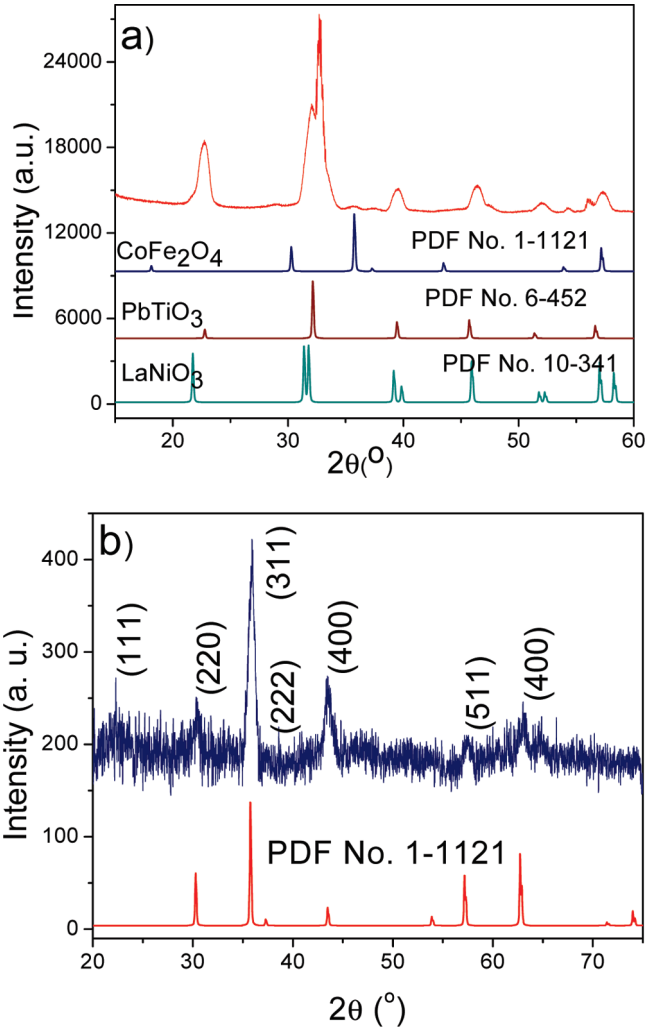

Figure 6. XRD profiles of (a) the PTO−CFO bilayered structure deposited on a $LaNiO_3$-buffered Si substrate and (b) the pure $Co_{0.32}Fe_{2.68}O_4$ film deposited onto a glass substrate.

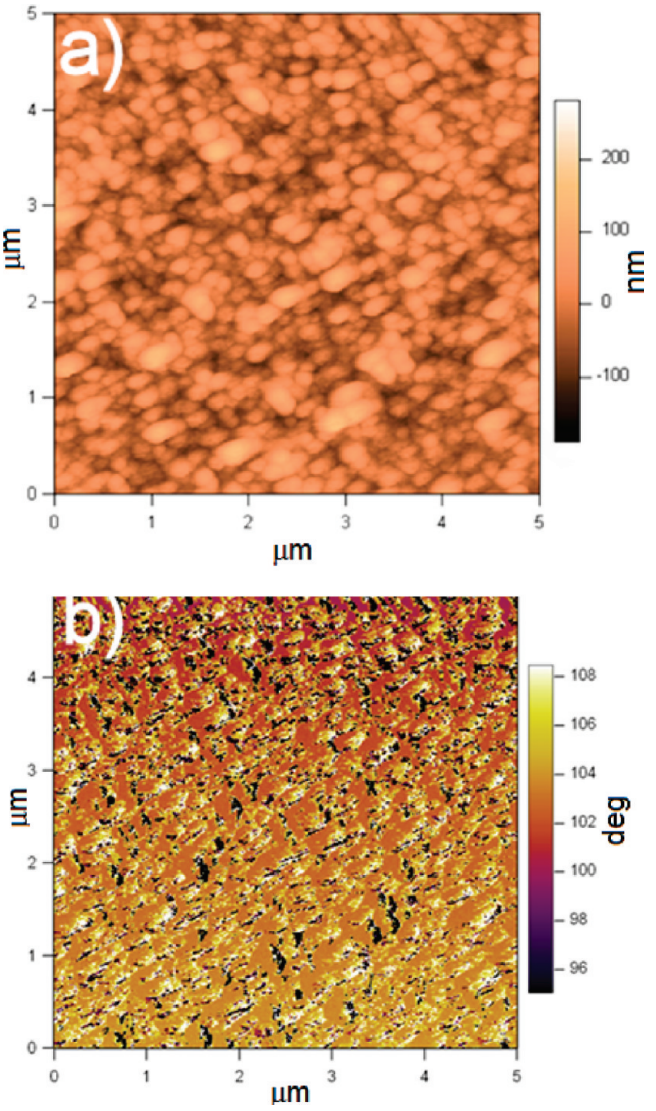

Figure 7. (a) Representative tapping-mode AFM and (b) MFM image of the ~180-nm-thick $Co_{0.32}Fe_{2.68}O_4$ top layer of the PTO−CFO bilayered structure.

bilayered nanocomposite is smaller than that of the pure CFO film ($H_c = 2.071$ KOe), which can be presumably ascribed to the coupling between the $Co_{0.32}Fe_{2.68}O_4$ and the $PbTiO_3$ phases at the shared interfaces. The saturation magnetization calculated after dissolving the film in diluted HCl solution, followed by weighing the sample and the glass substrate, is 234.4 emu/cm^3, which is lower than the value reported for bulk $CoFe_2O_4$ (~400 emu/cm^3).[24]

To further demonstrate the feasibility of this method, a second series of bilayered structures, consisting of a 200-nm-thick nickel ferrite (NFO) film deposited onto the initial PTO film, was fabricated by the same experimental procedure. Similar to the CFO film, the 2θ scans XRD scans (not shown) indicated that both the PTO and NFO layers are single-phase and are polycrystalline with the absence of any preferential orientation. ICP measurements of samples collected by dissolving randomly selected areas of the film (by masking it with cellophane tape and immersing it in a diluted HCl solution) indicated that the NFO layer is compositionally uniform and corresponds to the composition $Ni_{0.66}Fe_{2.34}O_4$. The FE-SEM micrograph of the PTO-NFO nanocomposite film (Figure 9) shows that, unlike the $CoFe_2O_4$ film, the NFO top layer is constructed by rodlike nanoparticles with an average length of 200 nm and an average diameter of 15 nm. As seen in the top view FE-SEM image, the constituent nanoparticles of the NFO layer seem to have their long axes oriented out of the film plane. They are also densely packed and form a very uniform film that completely covers the PTO layer. The cross-sectional FE-SEM image of the PTO−NFO bilayered nanocomposite shows the $LaNiO_3$, PTO, and NFO layers. Generally, ceramic thin films grow in solution via two mechanisms: homogeneous nucleation and attachment of the nanoparticles and heterogeneous nucleation, respectively. Unlike homogeneous nucleation which usually results in the formation of films constructed by spherically shaped nanoparticles, heterogeneous nucleation occurs through surface-directed growth. This leads to preferential growth of the nucleated solid, resulting into the formation of

(24) Suzuki, Y.; Hu, G.; van Dover, R. B.; Cava, R. J. *J. Magn. Magn. Mater.* **1999**, *191*(1−2), 1–8.

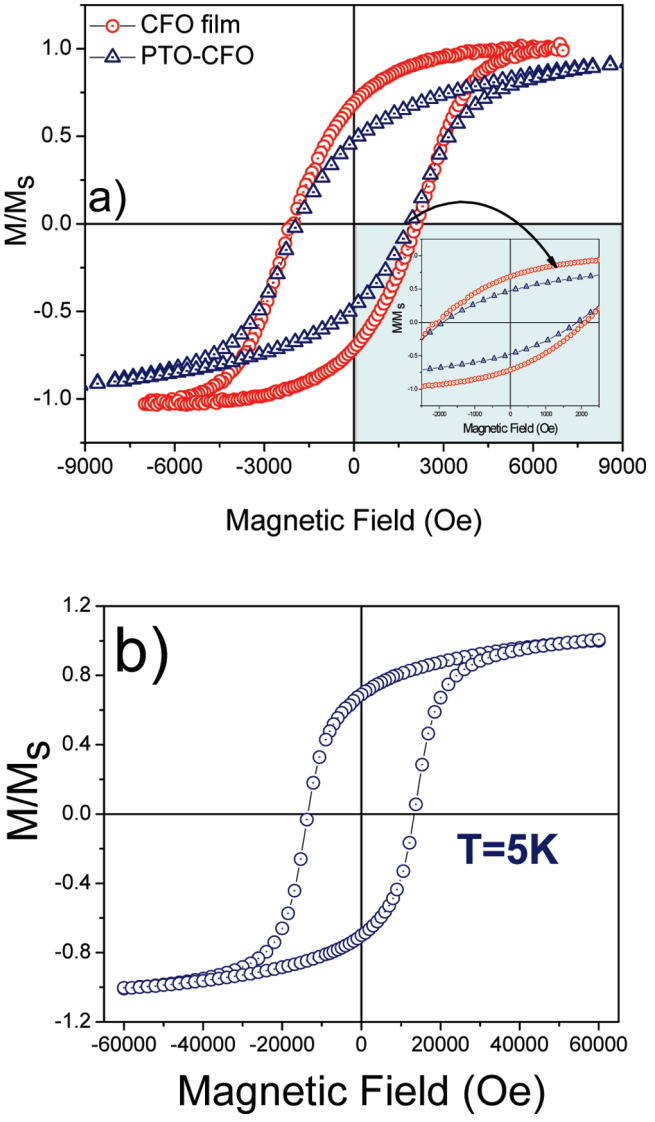

Figure 8. (a) Magnetization vs field curves at 300 K for the pure CFO film and the PTO−CFO bilayered structure. (b) Hysteresis loop of the PTO−CFO layered nanocomposite at 5 K. Magnetization values have been normalized to the value of the saturation magnetization.

columnar structures.[25] Regardless of the chemical composition of the ferrite films, in all experiments, the treatment solution turned progressively cloudy during the course of the hydrolysis process and turned clear again at the end of the deposition. However, because the morphology of the particles that comprise the ferrite film changes from spherical to rodlike, it results that, depending on their composition, the spinel films grow through both a homogeneous nucleation and a surface-directed heterogeneous nucleation mechanism. A systematic study on the influence of the nature of the transition metal, the concentration of the treatment solution/boric acid, and the deposition temperature on the morphology of the films is underway and will be reported in a forthcoming paper. The room-temperature magnetization curves of the pure NFO film and the bilayered PTO−NFO nanocomposite are shown in Figure 10. Similar to the PTO−

(25) Schwartz, R. W. *Chem. Mater.* **1997**, *9*, 2325.

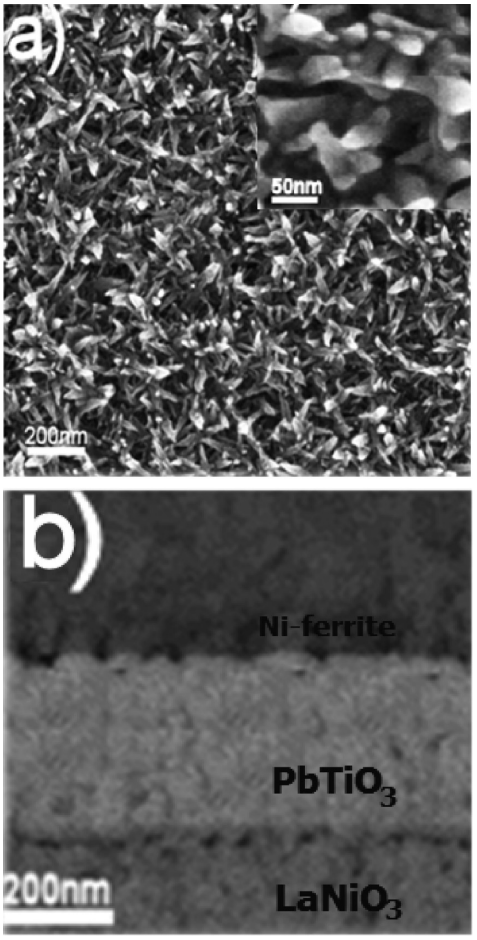

Figure 9. (a) Top-view FE-SEM image of the NFO thin film forming the top layer of the PTO−NFO multilayered structure (inset in upper right-hand corner shows an enlarged view). (b) Cross-sectional FE-SEM image of the PTO−NFO layered nanocomposite.

CFO nanocomposite films, no significant change in the coercivity and the orientation of the loops was noticed for measurements performed with the substrate oriented parallel and perpendicular to the magnetic field, indicating the existence of randomly oriented anisotropy axes. The saturation magnetization of the bilayered structure was 223.2 emu/g, which is a value that is smaller than both that of pure $Ni_{0.66}Fe_{2.34}O_4$ film (M_s = 241.5 emu/g) and that of bulk $NiFe_2O_4$ (M_s = 302.4 emu/g).[26] As in the case of the $CoFe_2O_4$ films, the decrease of the saturation magnetization of the $NiFe_2O_4$ layered structure can be ascribed to the existence of a noncolinear ferromagnetic spin structure in the vicinity of the surface of the individual nanoparticles constructing the film.[27] Unlike the PTO−CFO nanocomposite, the coercivity of the PTO−NFO layered nanocomposites is slightly higher (H_c = 108 Oe) than that of the pristine ferrite film (H_c = 90 Oe). These results were reproduced independently for three series of different samples and are in good agreement with those reported by Luo and co-workers for a $BaTiO_3$−$NiFe_2O_4$

(26) Caruntu, G.; Dumitru, I.; Bush, G. G.; Caruntu, D.; O'Connor, C. J. *J. Phys. D: Appl. Phys.* **2005**, *38*(6), 811–815.
(27) Robinson, I.; Volk, M.; Tung, L. D.; Caruntu, G.; Kay, N.; Thanh, N. T. K. *J. Phys. Chem. C* **2009**, *113*(22), 9497–9501.

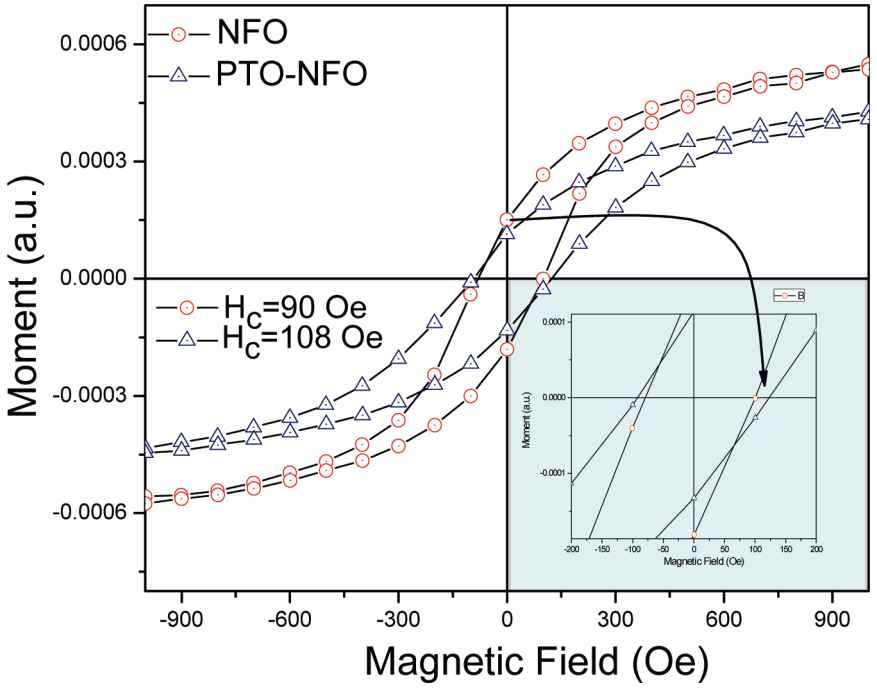

Figure 10. Room-temperature hysteresis loops of the pristine 200-nm-thick NFO film deposited on glass and the PTO−NFO bilayered nanocomposites.

epitaxial nanocomposite thin film obtained via a polymer-assisted deposition whereby the coercivity decreased from 150 Oe to 140 Oe, respectively.[9]

Raman spectroscopy has been proven to be a very versatile tool for the investigation of both the lattice dynamics in crystalline solids and the magnitude and types of residual stresses in ferroelectric thin film structures. The high-temperature cubic $PbTiO_3$ presents 12 optical modes that transform as the $3T_{1u}+T_{2u}$ irreducible representation of the point group O_h.[28] The triply degenerate T_{1u} mode is only infrared active, whereas the T_{1u} mode is neither Raman nor infrared active, being called "the silent mode". At room temperature, $PbTiO_3$ adopts a tetragonal structure and the T_{1u} optical lattice modes split into A_1+E, whereas the T_{2u} will split into B_1+E, respectively.[28,29] Because of long-range electrostatic interactions, the degeneracy of the lattice vibrations at long wavelengths is further lifted into a doubly degenerate transverse mode (TO), corresponding to an orientation of the polarization perpendicular to the wave vector **k** and a single longitudinal optical (LO) mode with polarization parallel to **k**. Similarly, the signature bands in the Raman spectra of ferrites are T_{2g} modes, corresponding to lattice vibrations in the MO_4 tetrahedra, and the A_{1g} modes, associated with vibrations of the octahedral sites of the cubic lattice.[30]

Figure 11 shows representations of the room-temperature Raman spectra of the PTO−CFO bilayered film with

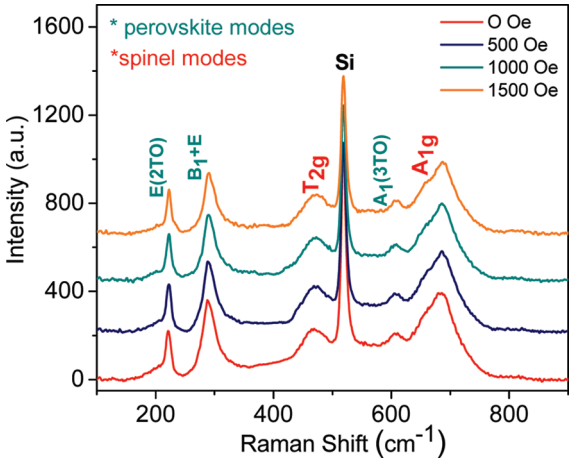

Figure 11. Raman spectra of the PTO−CFO bilayered structure in the absence (orange curve) and the presence (green, blue, and red curves) of a magnetic field with different intensities.

and without a magnetic field. To locate the Raman bands precisely, the spectra were deconvoluted with the PeakFit 4.12 software, using a linear baseline. The experimental data was smoothed with a four-order polynomial function (Savitsky−Golay) and the fitting process was performed with a Gaussian function. The reliability factors of each refinement procedure were >90%. As seen in Figure 11, three different types of peaks can be distinguished in each Raman spectrum: three bands at ~222, ~290, and ~609 cm^{-1}, which are ascribed to the E(2TO), B_1+E, and A_1-(3TO) vibrational modes of tetragonal $PbTiO_3$ (point group C_{4v}); a sharp, strong line at ~520 cm^1, which is characteristic to the silicon substrate; and two broad bands at ~472 and 687 cm^{-1}, corresponding to the T_{2g} and A_{1g} modes of the cubic spinel structure. The wavenumbers of the T_{2g} and A_{1g} modes of the spinel layer and the E(2TO), B_1+E and

(28) Pignolet, A.; Schmid, P. E.; Wang, L.; Levy, F. *J. Phys. D−Appl. Phys.* **1991**, *24*(4), 619–621.
(29) Taguchi, I.; Pignolet, A.; Wang, L.; Proctor, M.; Levy, F.; Schmid, P. E. *J. Appl. Phys.* **1993**, *73*(1), 394–399.
(30) (a) Wang, Z. W.; Schiferl, D.; Zhao, Y. S.; O'Neill, H. S. C. *J. Phys. Chem. Solids* **2003**, *64*(12), 2517–2523. (b) Casula, M. F.; Floris, P.; Innocenti, C.; Lascialfari, A.; Marinone, M.; Corti, M.; Sperling, R. A.; Parak, W. J.; Sangregorio, C. *Chem. Mater.* **2010**, *22*(5), 1739–1748. (c) Herranz, T.; Rojas, S.; Ojeda, M.; Pérez-Alonso, F. J.; Terreros, P.; Pirota, K.; Fierro, J. L. G. *Chem. Mater.* **2006**, *18*(9), 2364–2375.

Table 1. Values of the Raman Shift of the Perovskite and Spinel Layers in the PTO−CFO under a Magnetic Field

	Raman Bands					
	Ferrite Layer		Perovskite Layer			
coercivity, H (Oe)	T_{2g}	A_{1g}	E(2TO)	B_1+E	A_1(3TO)	Si
0	465.9	683.2	220.8	292.4	604.4	519.5
500	467.3	685.3	221.8	292.2	606.7	519.7
1000	469.6	686.3	222.7	292.2	608.2	519.6
1500	471.3	688.5	223.3	292.1	609.7	519.3

A_1(3TO) of the perovskite layer at different values of the in-plane magnetic field at room temperature are represented in Table 1. Upon increasing the magnetic field, the Raman modes of both the spinel and perovskite layers shift slightly toward higher frequency, whereas the position of the B_1+E band remains almost unchanged, suggesting that the silent mode is almost insensitive to the action of the magnetic field. Such behavior is similar to that observed by Li and co-workers for a Pb(Zr, Ti)O_3−$CoFe_2O_4$ bilayered structure obtained via a sol−gel method.[31] Because the shift of the Raman bands in thin-film structures is generally due to residual stresses,[32] the upward frequency shift in the Raman modes of both perovskite and spinel layers clearly indicates the existence of a stress-mediated magnetoelectric coupling in the PTO−CFO bilayered structure. Such a shift to higher frequencies of the ferrite Raman modes are ascribed to the convergent effect of changes in the lattice along and reorientation of the magnetic domains.[31] Under the action of an in-plane magnetic field, the ferrite layer, with a negative magnetostriction coefficient,[33] will shrink along the direction of the magnetic field. However, under a compression, the magnetic layer will expand slightly in a direction parallel to the normal of the film, generating a stress in the adjacent ferromagnetic layer. This stress, produced at the shared interfaces by the magnetoelastic effect, will change the configuration of the ferromagnetic domains in the perovskite phase, leading to a shift to higher frequencies of the E(2TO) and A_1(3TO) vibrational modes in the Raman spectrum. Although one can argue that the magnitude of the shift of the Raman modes is comparable to the instrumental resolution, the validity of the assumption that the shift in the Raman bands of the bilayered structure at $H \neq 0$ is associated with a stress-mediated ME coupling was further confirmed by the position of the Raman mode of the silicon substrate, which remains virtually unchanged upon applying the magnetic field. Similar results were observed in the PTO−NFO bilayered structure, which are consistent again with the existence of an elastic interaction between the perovskite and spinel layers in these bilayered ceramic nanocomposites obtained via LPD.

4. Conclusion

In summary, proof-of-concept experiments have demonstrated that it is possible to construct highly uniform polycrystalline $PbTiO_3$−$M_xFe_{3-x}O_4$ (M = Co, Ni) magnetoelectric (ME) bilayered nanocomposites, using the liquid-phase deposition process. This two-step procedure involves the sequential deposition of a $PbTiO_3$ film, followed by the formation of a transition-metal ferrite layer at temperatures as low as 45 °C. The resulting bilayered structures possess a granular morphology, are chemically pure, and are coupled through an elastic interaction, as evidenced by electron microscopy, X-ray diffraction, and magnetic field-assisted Raman spectroscopy. The general potential of the proposed route is multifold, because it allows the direct assembly of spinel and perovskite multicomponent metal oxide compositions into hierarchical multilayered structures via a simple chemical approach. At the same time, it allows for strict control over the number of perovskite/spinel layers, as well as their thickness and chemical composition. These hybrid nanostructures, in a film-on-substrate geometry, will open the door to more-detailed studies on their electrical and magnetic properties and stimulate the design of other combinations of spinel and perovskite phases in a planar geometry.

Acknowledgment. This work was financially supported by the Advanced Materials Research Institute (through a DARPA Grant No. HR 0011-09-1-0047). A.K.P. thanks the Office of Sponsored Research Projects at the University of New Orleans for financial support. Authors are indebted to Dr. Aurelian Rotaru for useful discussions about the magnetic properties of the films.

(31) Li, Z.; Wang, Y.; Lin, Y. H.; Nan, C. Phys. Rev. B **2009**, *79*, No. 180406.
(32) (a) Sanjurjo, J. A.; Lopezcruz, E.; Burns, G. *Phys. Rev. B* **1983**, *28* (12), 7260–7268. (b) Cheng, J. R.; He, L.; Yu, S. W.; Meng, Z. Y. Appl. Phys. Lett. **2006**, *88*, No. 152906.
(33) Bhame, S. D.; Joy, P. A. *J. Phys. D−Appl. Phys.* **2007**, *40*(11), 3263–3267.